AGU PUBLICATIONS

Paleoceanography

RESEARCH ARTICLE
10.1002/2015PA002862

Key Points:
- Changes in biogenic and dust fluxes are simultaneous, suggesting wind strength as the primary driver
- Biogenic fluxes reach maxima during abrupt coolings, suggesting stronger trade winds
- Biogenic fluxes are lowest during the African Humid Period, suggesting weakened trade winds

Supporting Information:
- Caption for Data Set S1
- Data Set S1

Correspondence to:
L. I. Bradtmiller,
lbradtmi@macalester.edu

Citation:
Bradtmiller, L. I., D. McGee, M. Awalt, J. Evers, H. Yerxa, C. W. Kinsley, and P. B. deMenocal (2016), Changes in biological productivity along the northwest African margin over the past 20,000 years, *Paleoceanography*, *31*, 185–202, doi:10.1002/2015PA002862.

Received 16 JUL 2015
Accepted 23 DEC 2015
Accepted article online 29 DEC 2015
Published online 23 JAN 2016

Changes in biological productivity along the northwest African margin over the past 20,000 years

Louisa I. Bradtmiller[1], David McGee[2], Mitchell Awalt[1], Joseph Evers[1], Haley Yerxa[1], Christopher W. Kinsley[2,3], and Peter B. deMenocal[4,5]

[1]Department of Environmental Studies, Macalester College, St. Paul, Minnesota, USA, [2]Department of Earth, Atmospheric and Planetary Sciences, Massachusetts Institute of Technology, Cambridge, Massachusetts, USA, [3]Woods Hole Oceanographic Institution, Woods Hole, Massachusetts, USA, [4]Department of Earth and Environmental Sciences, Columbia University, New York, New York, USA, [5]Lamont-Doherty Earth Observatory, Columbia University, Palisades, New York, USA

Abstract The intertropical convergence zone and the African monsoon system are highly sensitive to climate forcing at orbital and millennial timescales. Both systems influence the strength and direction of the trade winds along northwest Africa and thus directly impact coastal upwelling. Sediment cores from the northwest African margin record upwelling-related changes in biological productivity connected to changes in regional and hemispheric climate. We present records of ^{230}Th-normalized biogenic opal and C_{org} fluxes using a meridional transect of four cores from 19°N–31°N along the northwest African margin to examine changes in paleoproductivity since the last glacial maximum. We find large changes in biogenic fluxes synchronous with changes in eolian fluxes calculated using end-member modeling, suggesting that paleoproductivity and dust fluxes were strongly coupled, likely linked by changes in wind strength. Opal and C_{org} fluxes increase at all sites during Heinrich Stadial 1 and the Younger Dryas, consistent with an overall intensification of the trade winds, and changes in the meridional flux gradient indicate a southward wind shift at these times. Biogenic fluxes were lowest, and the meridional flux gradients were weakest during the African Humid Period when the monsoon was invigorated due to precessional changes, with greater rainfall and weaker trade winds over northwest Africa. These results expand the spatial coverage of previous paleoproxy studies showing similar changes, and they provide support for modeling studies showing changes in wind strength and direction consistent with increased upwelling during abrupt coolings and decreased upwelling during the African Humid Period.

1. Introduction

Paleoclimate records from North Africa show that continental and marine climate during the African Humid Period (AHP; 11.7–5 ka) was very different from the modern, resulting from nonlinear responses to gradual insolation forcing [e.g., *Adkins et al.*, 2006; *deMenocal et al.*, 2000b; *McGee et al.*, 2013; *Prell and Kutzbach*, 1987; *Shanahan et al.*, 2015]. Many reconstructions also record rapid changes in African climate linked to abrupt cooling events in the North Atlantic, such as the Younger Dryas (YD; 12.9–11.7 ka) and Heinrich Stadial 1 (HS1; ~17.5–15 ka) [e.g., *Adkins et al.*, 2006; *McGee et al.*, 2013; *Mulitza et al.*, 2008; *Romero et al.*, 2008; *Weldeab et al.*, 2011; *Zarriess and Mackensen*, 2010]. North African climate is highly sensitive to changes in the intensity and northward penetration of the African monsoon system, which is embedded within the northern cell of the Hadley circulation and the Intertropical Convergence Zone (ITCZ).

The trade winds—the surface expression of the Hadley circulation—along with coastal geometry determine the strength and location of coastal upwelling zones along the northwest African margin. The strength and location of coastal upwelling help to determine coastal sea surface temperature (SST), which has been shown to provide a positive feedback to orbital and millennial-scale changes in the monsoon [*deMenocal et al.*, 2000b; *Liu et al.*, 2014; *Mulitza et al.*, 2008; *Tjallingii et al.*, 2008]. The strength of upwelling also partially determines the availability of nutrients at the ocean surface and, by extension, the surface production and sedimentary accumulation of biogenic materials. Records of the accumulation of upwelling-driven biogenic sediments along the northwest African margin thus provide an important means of reconstructing the response of regional winds to high- and low-latitude influences over orbital and millennial timescales [*Freudenthal et al.*, 2002; *Kuhlmann et al.*, 2004b; *Martinez et al.*, 1999; *Mulitza et al.*, 2008; *Tjallingii et al.*, 2008].

During the AHP, precessional increases in local summer insolation peaking at 10 ka [*Berger and Loutre*, 1991] resulted in an intensification of the monsoon [*Prell and Kutzbach*, 1987] and northward migration of both the ITCZ over the eastern tropical Atlantic and the rain belt over North Africa. North Africa contained several large perennial lakes ranging in latitude from 13°N to 34°N [*Gasse*, 2000; *Hoelzmann et al*., 1998, 2004; *Kropelin et al*., 2008; *Street-Perrott and Harrison*, 1984; *Street-Perrott and Perrott*, 1993], the approximate range of the modern Sahara desert. The region also supported human settlements in this same latitudinal range, as evidenced by archeological data [*Kuper and Kropelin*, 2006; *Manning and Timpson*, 2014]. Fluvial discharge was greatly increased, while dust fluxes were dramatically reduced, as reflected in Gulf of Guinea paleosalinity data and by changes in the relative abundance of coarse-grained (eolian) and fine-grained (fluvial) detrital sedimentary fluxes to ocean sediments [*Adkins et al*., 2006; *Kuhlmann et al*., 2004a; *McGee et al*., 2013; *Mulitza et al*., 2008; *Tjallingii et al*., 2008; *Weldeab et al*., 2007]. Foraminiferal and diatom assemblages indicate decreased upwelling (and upwelling-derived productivity) during the AHP, and alkenone-derived records of SST show increased temperatures [*Abrantes*, 2000; *Romero et al*., 2008; *Zarriess and Mackensen*, 2010; *Zhao et al*., 1995]. All available data are consistent with North Africa having been exceptionally wet during this period.

The termination of the AHP resulted from an orbital decrease in boreal summer insolation which caused a southward retreat of the monsoonal rains and an ensuing reversal in the balance of evaporation and precipitation for North Africa. Some paleolacustrine records and fluvial discharge indices suggest gradual decreases in monsoonal precipitation between 6 and 4 ka B.P. [*Gasse et al*., 1990; *Kropelin et al*., 2008; *Street-Perrott and Harrison*, 1984], and a recent data compilation suggests a time transgressive end of the AHP spanning several thousand years, with sites in the north drying first [*Shanahan et al*., 2015]. In contrast, sediments from Ocean Drilling Program (ODP) Site 658 (21°N) record a doubling of dust fluxes within a few centuries of the termination of the AHP near 5 ka [*Adkins et al*., 2006]. Recent work on the transect of sediment cores discussed here further indicates rapid, century-scale increases in ^{230}Th-normalized dust fluxes near 5 ka B.P. across a large latitudinal range spanning 19°–27°N [*McGee et al*., 2013]. However, there is some debate as to whether the observed dust flux changes primarily reflect changes in regional aridity and vegetation density or changes in the competence of the transporting winds. We address this issue here.

Abrupt stadial cooling events in the North Atlantic region are clearly imprinted on North African monsoonal climate records. During HS1, dust fluxes were greatly elevated along the Mauritanian coast [*McGee et al*., 2013] and SSTs decreased [*Romero et al*., 2008; *Zhao et al*., 1995]. An index of humidity based on the grain size of terrigenous material in marine sediments suggests that HS1 was the most arid period in the past ~30 ka [*Tjallingii et al*., 2008]. Foraminiferal and diatom assemblages indicate increased upwelling (and upwelling-derived productivity) during HS1, and bulk geochemical data lend support to the presence of both increased dust as well as increased biogenic fluxes to the sediment [*Abrantes*, 2000; *Kuhlmann et al*., 2004b; *Martinez et al*., 1999; *Mulitza et al*., 2008; *Romero et al*., 2008; *Sarnthein et al*., 1981; *Zarriess and Mackensen*, 2010]. All of these lines of evidence are consistent with a southward shift and intensification of the northern trade winds as a result of rapid cooling of the North Atlantic and the associated decrease in North Atlantic deepwater formation [*McManus et al*., 2004; *Mulitza et al*., 2008]. Climate models have likewise suggested that such a southward shift of the Hadley Cell would be accompanied by an increase in trade wind strength [*Broccoli et al*., 2006]. However, there is some uncertainty as to whether decreased SSTs along the northwest African margin during HS1 were due to (1) the southward advection of colder North Atlantic water, (2) increased upwelling, or (3) both [*Bard*, 2002; *Chapman et al*., 2000; *Claussen et al*., 2003; *deMenocal et al*., 2000a; *Street-Perrott and Perrott*, 1990; *Zhao et al*., 1995, 2006].

The Bølling-Allerød warm period (BA; 14.7–12.9 ka) in the North Atlantic manifested as a time of decreased dust fluxes [*McGee et al*., 2013; *Mulitza et al*., 2008] and increased SSTs [*Romero et al*., 2008] along the northwest African margin. Bulk sedimentary Al/Si and Fe/K records also indicate generally more humid conditions [*Mulitza et al*., 2008], all of which is consistent with a more northerly mean position of the African monsoonal rain belt. In contrast, the Younger Dryas strongly resembles HS1 with respect to elevated dust fluxes [*Adkins et al*., 2006; *McGee et al*., 2013], increased upwelling-derived biological productivity [*Adkins et al*., 2006; *Romero et al*., 2008], lower humidity [*Mulitza et al*., 2008; *Tjallingii et al*., 2008; *Weldeab et al*., 2007], and lower SSTs [*Romero et al*., 2008; *Zhao et al*., 1995, 2000].

Here we present paleoproductivity records over the last 20 ka from a latitudinal transect of four cores along the northwest African margin. Our ^{230}Th-normalized flux records of biogenic opal and organic carbon (C_{org})

document spatial and temporal changes in the strength of upwelling-derived biological productivity associated with orbital and millennial-scale changes. By examining paleoproductivity records from the coastal upwelling system we seek to identify the influence of changes in wind patterns and to test whether productivity changes documented in single cores reflect coherent regional-scale patterns [*Adkins et al*., 2006; *Bertrand et al*., 1996; *Romero et al*., 2008].

We combine our results with records of eolian dust flux in the same cores [*McGee et al*., 2013] in order to address the magnitude and timing of changes in regional climate, wind fields, and associated coastal upwelling over the past 20 ka. By comparing the magnitudes of changes in two upwelling-derived biological proxies to changes in dust fluxes in the same cores we hope to distinguish between several of the major forcings common to all three proxies. If dust fluxes and biogenic fluxes are principally influenced by wind strength and position, we would expect records of all three proxies to look similar through time at each site. However, if dust fluxes are more significantly affected by regional paleohydrologic changes and vegetation cover, or if biogenic fluxes are more sensitive to changes in the source and nutrient content of the upwelled water, then we might expect the biogenic and dust records to differ significantly. Finally, the latitudinal transect allows us to examine meridional changes in regional climate, wind strength, and coastal upwelling along the margin. In particular, changes in the north-south gradient in opal and dust fluxes over time can be used to suggest latitudinal shifts in the northern trade wind position and intensity.

2. Regional Background

2.1. Core Locations and Regional Setting

We present new opal and organic carbon results from four cores on the northwest African Margin. Cores GC27, GC37, GC49, and GC68 were collected on the R/V *Oceanus* in 2007 as part of the Changing Holocene Environments in the Eastern Tropical Atlantic cruise (OC437-7). Cores range from 19°N to 31°N and span water depths of 1258 m to 2771 m (Table 1 and Figure 1). The southernmost cores (GC68 and GC49) are near the area of maximum modern winter upwelling and trade wind strength (Figure 1a), while the northernmost core (GC27) is in a region of relatively weak year-round winds [*Mittelstaedt*, 1991]. These differences in the wind regime are reflected in the values of Si* and chlorophyll concentration in near-surface (200 m) water shown in Figures 1c and 1d.

The strength and seasonality of upwelling along the northwest African margin are influenced directly by the trade winds, the lower limb of the northern hemisphere Hadley Cell. When the southern branch of the northeasterly trade winds blow parallel to the North African coast, they induce Ekman transport of water offshore. This water is subsequently replaced by cool nutrient-rich water from below. Over the ocean, the trades are controlled by the migration of the ITCZ due to changes in insolation on both seasonal and orbital timescales; changes in the relative heating of land and ocean may also play a role in coastal wind strength and orientation [*Bakun*, 1990]. The modern Atlantic ITCZ reaches its northernmost position (~15°N) during boreal summer, which causes strong trade winds from 20−32°N. During boreal winter the ITCZ shifts south to approximately 5°N in the northwest margin region, and trade winds are strongest between 10 and 25°N at this time [*Van Camp et al*., 1991]. Actual wind-driven upwelling is limited to a relatively narrow (20–30 km) band along the shelf, but the influence of the upwelling system as indicated by low SSTs extends as far as 200–300 km from the coast [*Mittelstaedt*, 1991]. However, maximum accumulation of biogenic fluxes occurs on the slope at depths from 1000 to 1500 m due to shelf transport processes [*Bertrand et al*., 1996; *Martinez et al*., 1999]. Our cores range from 75 to 160 km from the modern coast, or 30 to 80 km from the 120 m isobath, which approximates the LGM coastline (Table 1) [*McGee et al*., 2013]. Cores range from 1258 m to 2771 m water depth.

The seasonality of modern upwelling varies significantly with latitude. South of 20°N upwelling is strongest in the winter and spring. From 20 to 25°N upwelling is strong year round, with maxima in the spring and autumn. North of 25°N upwelling is strongest during summer and early autumn [*Mittelstaedt*, 1991]. In general, the seasonality of upwelling is most pronounced south of Cape Blanc (20.8°N) and seasonality is relatively insignificant north of 25°N [*Mittelstaedt*, 1991]. There is a wind shadow near 30°N due to the presence of the Atlas Mountains that significantly decreases the overall strength of wind-driven upwelling in this area [*Mittelstaedt*, 1991].

Table 1. Core Locations, Depths, Linear Sedimentation Rates (LSRs), and Distances From Modern and LGM Shorelines [*McGee et al.*, 2013]

Core ID	Latitude (°N)	Longitude (°W)	Water Depth (m)	Mean LSR (cm/ka)	Distance to Modern Shoreline (km)	Distance to 120 m Isobath (km)
OC437-7 GC27	30.880	−10.630	1258	6.1	75	50
OC437-7 GC37	26.816	−15.118	2771	9.5	90	70
OC437-7 GC49	23.206	−17.854	2303	8.6	160	80
OC437-7 GC68	19.363	−17.282	1396	11	75	30

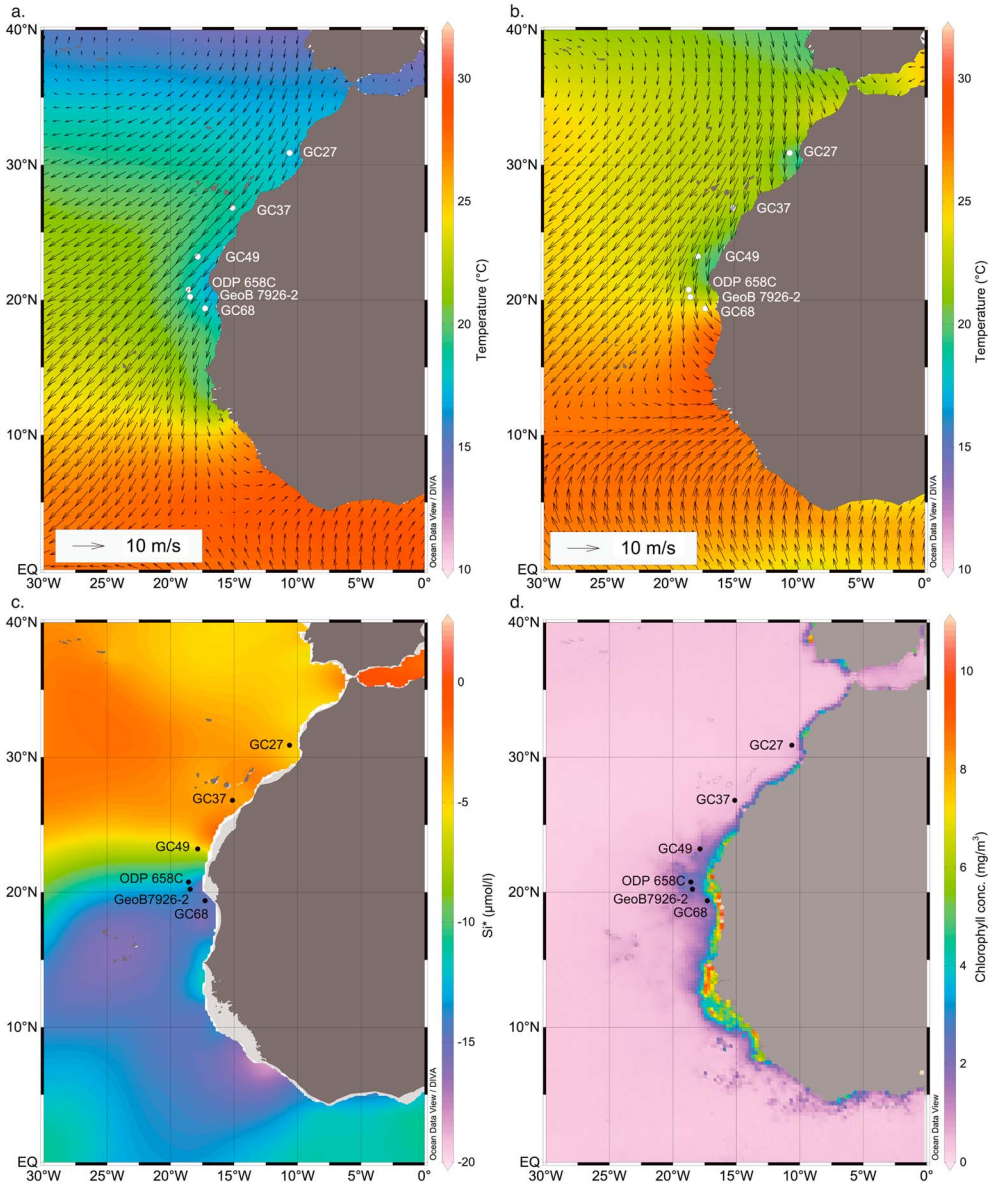

Figure 1. (a) Core locations shown over winter (January, February, and March) SST [*Locarnini et al.*, 2010] and February winds [*Zhang et al.*, 2006]. (b) Cores shown with summer (July, August, and September) SST [*Locarnini et al.*, 2010] and August winds [*Zhang et al.*, 2006]. (c) Core locations shown over the annual average of the quantity Si* ($[Si(OH)_4] - [NO_3^-]$; µmol/l) at 200 m water depth [*Garcia et al.*, 2010; *Sarmiento et al.*, 2004]. (d) Core locations shown over the concentration of chlorophyll (mg/m^3) at the surface [*NASA Goddard Space Flight Center, Ocean Ecology Laboratory, Ocean Biology Processing Group*, 2014]. The maps also include locations of cores ODP 658C [*Adkins et al.*, 2006; *deMenocal et al.*, 2000b] and GeoB7926-2 [*Romero et al.*, 2008].

The primary surface current in the region is the Canary Current, which flows south along the margin until it detaches between 20 and 25°N and gradually turns into the North Equatorial Current at lower latitudes [*Mittelstaedt*, 1991]. Beneath the Canary Current an undercurrent flows at least as far as 26°N, becoming deeper as it flows from south to north. As a result, south of approximately Cape Blanc the primary source of upwelled water is South Atlantic Central Water (SACW), which comes with the undercurrent. As the undercurrent reaches depths below the reach of the upwelling system (~300 m), the primary source of upwelled water becomes North Atlantic Central Water (NACW), which is relatively poor in nutrients compared to SACW [*Mittelstaedt*, 1991].

The convergence of the Canary Current and the North Equatorial Countercurrent at Cape Blanc results in a persistent filament of strong upwelling and therefore high productivity [*Helmke et al*., 2005]. This filament, identified by high concentrations of chlorophyll and low sea surface temperature, is strongest between 20 and 24°N and extends hundreds of kilometers offshore [*Van Camp et al*., 1991]. The location of the filament is determined in large part by the interaction between surface currents and coastal and shelf morphology, and so we must also consider how the location of the filament may have changed through time as changes in sea level altered coastal and shelf morphology. The modern shelf is narrow (~45 km wide), and the continental slope is also approximately 45 km wide with a slope of 2–3° [*Fütterer*, 1983]. During periods of decreased sea level, reductions in shelf area likely led to decreased filament formation, thereby decreasing export productivity transport to the slope and nutrient recirculation [*Holzwarth et al*., 2010].

2.2. Modern Interannual-to-Decadal Variability in Upwelling and Dust Emissions

Interannual and decadal-scale changes in upwelling along the northwest African margin can be inferred from wind speed data, SSTs from both satellite products and direct measurements, sea surface heights, and vertical water column velocities. Observations over the last 30 years (1981–2012) indicate that summer upwelling variability is out of phase to the north and south of ~21°N, as strengthening of the Saharan Heat Low drives stronger northeasterly winds in the north and onshore winds in the south. Some SST and wind data sets suggest a recent increase in summer upwelling north of 21°N and an increase in downwelling south of this boundary [*Cropper et al*., 2014]. This trend may have to do with recent strengthening of the Saharan Heat Low in summer [*Evan et al*., 2015], which has intensified the land-ocean pressure contrast [*Cropper et al*., 2014].

In contrast, winter upwelling variability is coherent throughout the NW African margin from ~12 to 35°N [*Cropper et al*., 2014]. This variability is correlated with the strength of the North Atlantic subtropical high, because winds on the southeastern edge of the high flow parallel to the coast during winter (i.e., northeasterly trade winds) [*Cropper et al*., 2014]. Accordingly, periods of strong subtropical high pressure (the positive phase of the North Atlantic Oscillation; NAO) lead to stronger winter winds and upwelling.

Dust deposition near the core sites occurs primarily in winter and early spring [*Bory and Newton*, 2000; *Neuer et al*., 1997; *Ratmeyer et al*., 1999]. As with winter upwelling, the positive phase of the NAO is positively correlated with dust aerosol optical depth along the northwest African margin in winter [*Chiapello et al*., 2005]. This variability appears to primarily reflect wind strength in the dust source areas rather than changes in precipitation or vegetation. *Doherty et al*. [2012] used Center of Action indices to characterize modern winter dust emissions data from west Africa and showed that southward shifts in the ITCZ lead to increased dust load in the atmosphere due to increased northeasterly winds over dust source regions. *Ridley et al*. [2014] modeled dust emissions from 1982 to 2008 using reanalysis meteorological data and demonstrated that decreasing surface winds were the primary driver of the decrease in dust emissions over this time period. Precipitation and vegetation changes in dust source areas played a very minor role in summer emissions and had no effect in winter.

Modern observations provide a useful template for interpreting proxy data related to upwelling and dust deposition on the northwest African margin. If variations in summer climate are the main driver of changes in upwelling, then proxy data should show a dipole response centered around 21°N; the position of this boundary may shift due to changes in the latitudinal position of the Saharan Heat Low and Atlantic subtropical high. Variations in summer winds might not be reflected in the dust record given the modern dominance of winter and spring dust deposition along our transect. Changes in winter climate should produce coherent upwelling variability along the margin and may also be correlated with dust deposition, as both winter upwelling and dust deposition vary with northeasterly wind strength in the modern climate.

3. Methods

3.1. Analytical Methods

The age models for these cores have been previously described by *McGee et al*. [2013]; additional details, radiocarbon ages, and complete age models can be found in the original reference and accompanying supporting information. Core chronologies were developed using AMS radiocarbon ages on planktonic foraminifera using monospecific samples (*Globigerina bulloides*) whenever possible. Radiocarbon measurements were made at the Center for Accelerator Mass Spectrometry at Lawrence Livermore National Laboratory, and ages were converted to calendar years using the Marine13 data set [*Reimer et al*., 2013] and a ΔR of 130 ± 50 years (2σ) based on modern local reservoir ages [*Ndeye*, 2008]. An age model for each core was interpolated between radiocarbon ages using the P_Sequence routine in Oxcal 4.1, a Bayesian age-depth modeling routine [*Bronk Ramsey*, 2009]. Note that radiocarbon dates in *McGee et al*. [2013] were converted to calendar years using the Marine09 data set. The recalibration results in only minor changes to the age models used here. In core GC 37, modeled ages from 14.5 to 12 kyr (new age model) are on average 300 years younger than in the original. In core GC68 modeled ages during the LGM are on average 200 years older, and ages during HS1 are 150 years younger than the original model. The difference between age models in all other cores and at all other depths was less than 100 years.

The reservoir age of waters likely changed significantly over the period of study; previous work suggests that the average marine reservoir correction in the North Atlantic was as high as 700 years during the YD (i.e., ΔR of 300) [*Bard et al*., 1994] and was possibly even larger along the African Margin due to increased upwelling [*deMenocal et al*., 2000b]. We tested the sensitivity of our age model during key intervals (LGM, YD, and H1) using ΔR as high as 500 (i.e., a reservoir age of 900 years). While the resulting age models changed as expected, with age estimates shifting younger, these changes were not enough to move samples from one interval to another (e.g., all samples previously defined as being within H1 remained in H1 using the new age model). However, the combination of uncertainty in ΔR and the effects of bioturbation does leave open the possibility that some opal peaks that likely represent the YD appear to occur at the end of the BA warm period (e.g., GC49) [*McGee et al*., 2013]. While a full treatment of changes in reservoir age over time at these sites is outside the scope of this work, we are confident that our primary conclusions regarding changes in biogenic accumulation during these time periods are robust with respect to uncertainty in the age models.

Percent biogenic opal was determined using alkaline extraction and molybdate blue spectrophotometry after the method of *Mortlock and Froelich* [1989]. An internal standard was run with each rack of 22 samples resulting in a reproducibility of 4.1% relative standard deviation (RSD), relative to the measured value. Percent carbonate and percent total carbon were determined through coulometry. Replicates were run for 43 carbonate samples with an average error of 3.8% RSD. Total carbon samples were all duplicated; the average error was 3.2% RSD, and the average of all replicates for a given sample was used to calculate percent organic carbon. Percent organic carbon was calculated as the difference between total carbon and carbonate carbon.

Total sediment flux for all samples was determined by ^{230}Th normalization. Most uranium and thorium isotope concentrations were previously published by D. McGee [*McGee et al*., 2013]; newly collected data from GC37 are indicated in the supporting information. Uranium (^{238}U and ^{234}U) and thorium (^{232}Th and ^{230}Th) concentrations were determined by isotope dilution using an Axiom single-collector ICP-MS at LDEO [*McGee et al*., 2013] and a Thermo Scientific Neptune Plus multicollector ICP-MS at Brown University (this study) [*Anderson and Fleer*, 1982; *Fleisher and Anderson*, 2003]. Uncertainties on isotopic compositions are ~1%, and the reproducibility of ^{230}Th-based fluxes in an internal standard included in each set of samples is better than 4% RSD. The thorium normalization method is based on the assumption that the flux of particulate ^{230}Th sinking to the ocean floor is approximately equal to its known rate of production from ^{234}U decay in the water column because the residence time of ^{230}Th in the water column is relatively short (on the order of a few decades) [*Anderson et al*., 1983] compared to the rate of lateral mixing in deep ocean basins [*Anderson et al*., 1990]. Where burial rates of ^{230}Th are found to exceed its production in the water column, this is attributed to the lateral redistribution of sediments by deep-sea currents. The ^{230}Th normalization method has been supported by findings from both modeling [*Henderson et al*., 1999] and sediment trap studies [*Scholten et al*., 2001, 2005; *Yu et al*., 2001].

Using the total thorium normalized sediment flux, fluxes of individual sedimentary components can be calculated as $F_i = \frac{C_i \times \beta \times z}{xs^{230}Th_0}$, where F_i is the flux of a sedimentary constituent of interest, C_i is the concentration of that constituent in bulk sediment, and $\beta \times z$ is equal to the production rate of ^{230}Th in the water column (z is the depth of the

water column (cm) and $\beta = 2.63 \times 10^{-5}$ dpm cm^{-3} kyr^{-1}). The quantity xs^{230}Th$_0$ (dpm/g) is calculated by correcting the measured ^{230}Th concentration for ^{230}Th within detrital minerals, ^{230}Th supported by detrital and authigenic U, and radioactive decay. Corrections for ^{230}Th in detrital and authigenic U assume a ^{238}U/^{232}Th activity ratio of 0.7 ± 0.1 (1σ) in detrital minerals [*Adkins et al*., 2006].

Dust fluxes from these cores have been reported previously [*McGee et al*., 2013], but since they will be discussed here a brief description of the methods is included. See the original reference and accompanying supporting information for complete details. The terrigenous fraction of the sediment was first determined by subtracting measured concentrations of calcium carbonate, biogenic opal, and organic carbon. Terrigenous sediments at these sites are a mixture of relatively coarse-grained eolian dust and fine-grained sediment supplied by rivers and remobilized from the continental shelf. End-member modeling of the grain size distribution of terrigenous sediments was used to estimate the eolian fraction of terrigenous sediments in each sample. To isolate the operationally defined terrigenous fraction for grain size analysis, biogenic sediments were first removed using a modification of the method of *Mulitza et al*. [2008]. Grain size measurements were subsequently conducted using an LS200 Coulter laser particle size analyzer at the University of Bremen. *McGee et al*. [2013] fit the grain size data using Weibull distributions and used a three-end-member model to describe the downcore variability. The finest end-member (EM3 mode = 4–6 μm) was interpreted as reflecting fluvial or resuspended sediments, while the coarser two end-members (EM2 mode = 20–30 μm; EM1 mode >60 μm) were combined to represent eolian sediments [*Mulitza et al*., 2008; *Tjallingii et al*., 2008].

3.2. Biogenic Upwelling Proxies

Opal forms primarily as the siliceous frustules of diatoms and is therefore an indicator of export productivity. While the majority of opal produced in the surface ocean is dissolved before reaching the seafloor [*Nelson et al*., 1995; *Treguer et al*., 1995], several studies have reported that the presence of large, dissolution-resistant species (*Thalassionema nitzschioides* and *Chaetoceros*) in upwelling regimes [*Gil et al*., 2007; *Koning et al*., 2001] makes sedimentary opal flux a suitable proxy for diatom surface productivity in those areas. Opal fluxes have furthermore been shown to reflect spatial patterns of primary productivity in regions of strong upwelling in the equatorial Atlantic [*Bradtmiller et al*., 2007]. Study of a nearby core indicates that there was no preferential dissolution of opal during the LGM [*Romero et al*., 2008]; light microscopy showed good preservation and only minor dissolution effects on the main species present. Opal is also produced by other groups, most notably as the shells of radiolaria and in the form of sponge spicules. Additionally, opal in African margin sediments can also originate from freshwater diatoms blown from dried lake beds into the ocean. However, these inputs are relatively small; the contribution of radioalaria and sponge spicules to total opal burial is thought to be minimal except in specific environments [*Tréguer and De La Rocha*, 2013], and even during large dust events, the abundance of freshwater diatoms is still an order of magnitude less than the abundance of marine diatoms during moderately productive periods [*Romero et al*., 2008; *Skonieczny et al*., 2011].

The rain of C_{org} to the sea floor depends strongly on both opal and carbonate fluxes. Although early statistical analyses identified a global correlation between the fluxes of C_{org} and of $CaCO_3$ [*Francois et al*., 2002; *Klaas and Archer*, 2002], other studies indicate a stronger mechanistic relationship between diatom productivity and the flux of C_{org} to the deep sea. This relationship exists primarily because the fraction of net primary production that is exported from the euphotic zone is strongly correlated with the abundance of large phytoplankton taxa, especially diatoms [*Buesseler*, 1998; *Buesseler et al*., 2007; *Guidi et al*., 2009; *Honda and Watanabe*, 2010]. One reason for this is that opal also serves as an effective ballast to enhance the transfer of C_{org} to the deep sea [*Boyd and Trull*, 2007; *Honda and Watanabe*, 2010]. However, carbonate can also serve as an effective ballast for C_{org}; a sediment trap study off of nearby Cape Blanc suggests that there is a particularly strong statistical relationship between carbonate and C_{org} fluxes ($r^2 = 0.75$) in this area [*Helmke et al*., 2005]. While dust is not a significant source of ballast material in most of the ocean, it plays an important but secondary role in this region; the same study found $r^2 = 0.3$ for the regression between lithogenic and C_{org} fluxes and $r^2 = 0.89$ for the regression between total mineral ballast (carbonate, lithogenic, and opal) and C_{org} fluxes [*Helmke et al*., 2005]. *Fischer and Karakaş* [2009] note that primary productivity in the region is dominated by coccolithophorids, which export disproportionately high amounts of C_{org} relative to other carbonate producers. In the context of this work, we note that two primary scenarios might result in increased C_{org} fluxes to the sediment: increased wind-driven upwelling, which would increase nutrient availability generally, or an increase in the Si content of upwelled water, which might allow for more diatom export of C_{org}. A combination of these scenarios is also

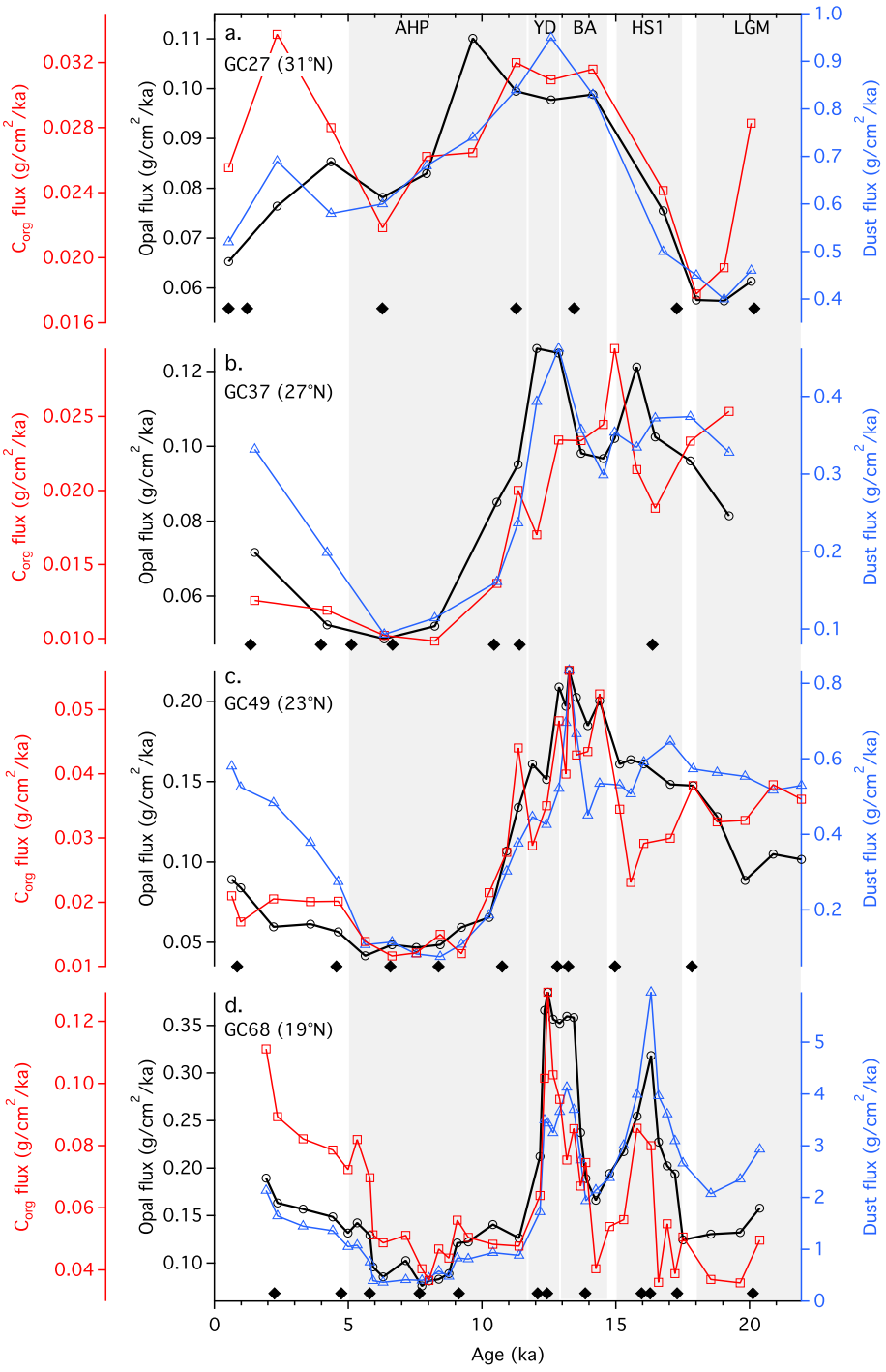

Figure 2. Fluxes of opal, C_{org}, and dust in cores (a) GC27, (b) GC37, (c) GC49, and (d) GC68. Dust fluxes are from *McGee et al.* [2013]. Locations of radiocarbon tie points for each core are indicated by black diamonds.

possible but would be difficult to differentiate using this suite of proxies. Where data exist, we also compare our biogenic proxies with SST reconstructions as an independent indicator of upwelling.

4. Results

Opal and C_{org} fluxes generally decrease from south to north throughout the last 20 ka, in good agreement with the modern upwelling climatology in the region [*Mittelstaedt*, 1991]. Opal fluxes in northernmost core

GC27 (Figure 2a) show an opal flux minimum during the late glacial period (~0.06 g cm^{-2} kyr^{-1}) followed by a gradual increase toward peak values from 14.1 to 9.7 ka (0.10–0.11 g cm^{-2} kyr^{-1}). Opal fluxes then decrease in a stepwise pattern throughout the Holocene. Fluxes of organic carbon show a similar pattern, with a late glacial minimum (0.02 g cm^{-2} kyr^{-1}) followed by an increase toward values above 0.03 g cm^{-2} kyr^{-1}. After a brief decrease, however, organic carbon fluxes increase during the late Holocene to 0.03 g cm^{-2} kyr^{-1}. Both opal and organic carbon fluxes show a similar temporal pattern to previously published dust flux data [*McGee et al*., 2013] also included in Figure 2.

Core GC37 (Figure 2b) shows peaks in opal flux during HS1 (0.12 g cm^{-2} kyr^{-1}) and the YD (0.13 g cm^{-2} kyr^{-1}). Opal fluxes then decrease gradually to a minimum at 6.3 ka (0.05 g cm^{-2} kyr^{-1}) and increase again into the late Holocene. Organic carbon fluxes show a peak of 0.03 g cm^{-2} kyr^{-1} during HS1 and a minimum value of 0.01 g cm^{-2} kyr^{-1} at 8.2 ka but do not record a distinct YD peak. The dust flux record [*McGee et al*., 2013] strongly resembles the opal flux record in this core as well, albeit with a muted peak during HS1 and a larger relative increase into the late Holocene than the other two proxies.

Opal fluxes in GC49 increase in a stepwise pattern from late glacial values of approximately 0.1 g cm^{-2} kyr^{-1} to a peak value of 0.22 g cm^{-2} kyr^{-1} at 13.2 ka, with high fluxes persisting into the YD (Figure 2c). Opal fluxes then decrease sharply until 10.3 ka and continue to decrease gradually until reaching a minimum value of 0.04 g cm^{-2} kyr^{-1} at 5.6 ka. Opal fluxes increase slightly throughout the uppermost part of the core. Organic carbon fluxes exhibit elevated fluxes immediately prior to and during the YD (0.06 g cm^{-2} kyr^{-1}), a minimum during the AHP (0.01 g cm^{-2} kyr^{-1}) and an abrupt increase during the termination of the AHP between 5.6 and 4.6 ka. The dust flux record from this core [*McGee et al*., 2013] closely resembles the opal and organic carbon records, with the exception that dust fluxes show a small peak associated with HS1.

Opal fluxes in GC68, the southernmost core, show the greatest variability over time (Figure 2d). Fluxes are relatively low (0.13 g cm^{-2} kyr^{-1}) during the late glacial period (19 ka) and increase to 0.31 g cm^{-2} kyr^{-1} at 16.3 ka, coincident with HS1, before decreasing again to values near 0.17 g cm^{-2} kyr^{-1} during the BA. Fluxes are highest during the YD (0.39 g cm^{-2} kyr^{-1}; 12.5 ka) and then decrease rapidly to fluxes similar to that of the late glacial. Fluxes decrease slightly between 9.0 and 7.7 ka, after the onset of the AHP, and increase slightly between 5.9 and 5.3 ka, near the AHP termination. Opal fluxes increase steadily after the end of the AHP throughout the late Holocene, reaching a value of 0.19 g cm^{-2} kyr^{-1} at the coretop. The flux of organic carbon follows a very similar pattern to that of opal flux, with a maximum flux of 0.13 g cm^{-2} kyr^{-1} during the YD and minima of 0.04 g cm^{-2} kyr^{-1} at 8 ka and during the late glacial. Opal and organic carbon fluxes again show a very similar temporal pattern to previously published dust flux data [*McGee et al*., 2013].

Calcium carbonate fluxes in all four cores (not shown) primarily vary between 0.8 and 1.2 g cm^{-2} kyr^{-1} [*McGee et al*., 2013]. All cores show a consistent pattern, with low fluxes during the late glacial, a broad peak during the deglaciation, and low, stable fluxes during the Holocene. While the carbonate data are not discussed in detail on their own, we employ the ratio of opal:carbonate flux later in the discussion and so include this brief description for context. Opal and carbonate fluxes are both susceptible to alteration during the burial process through dissolution and/or remineralization. As such, the sedimentation rate often plays a large role in the preserved flux of these sedimentary components, with high sedimentation rates leading to relatively greater preservation (see discussion below). We regressed opal fluxes against the linear sedimentation rate (LSR) within each core to gain a first-order understanding of the relationship between the two. The r^2 value for the correlation between opal flux and LSR in core GC49 was by far the greatest (0.78), while the other three cores all showed r^2 values below 0.5 (GC27 = 0.01; GC37 = 0.48; GC68 = 0.41). This suggests that we need to interpret the records from the three cores from the modern upwelling region with an awareness of the effects of changing sedimentation rates, most especially core GC49.

5. Discussion

5.1. Millennial-Scale Events

Our records of opal and C_{org} flux are consistent with much of the previous work on the West African monsoon and upwelling systems on both orbital and millennial timescales, and the latitudinal transect allows us to document the spatial fingerprint of past changes. Broadly, the cores show in-phase variability in biogenic sediment fluxes from 19 to 27°N over the past 20,000 years. During HS1 cores GC68 and GC37 show distinct

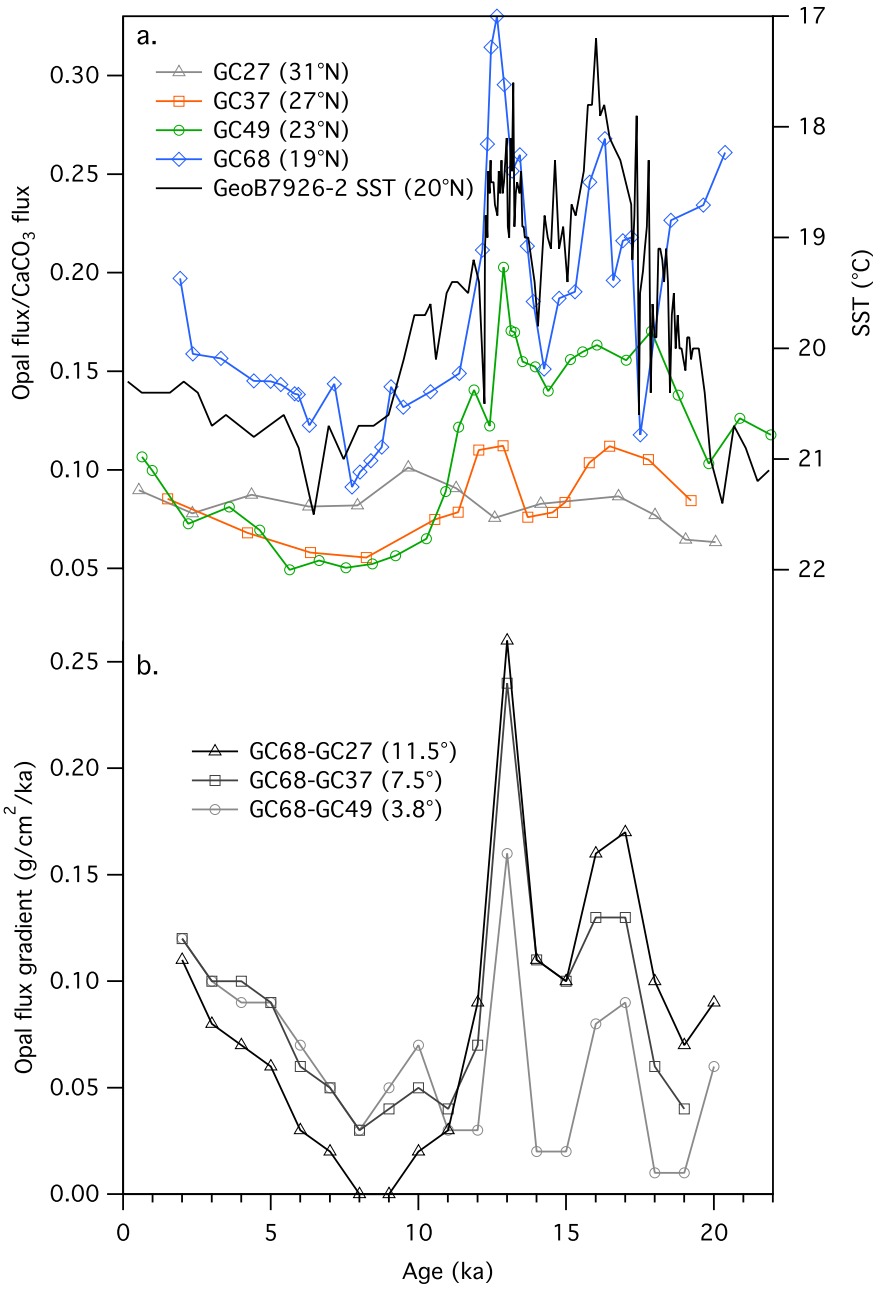

Figure 3. The ratio of opal:$CaCO_3$ in cores (a) GC68, GC49, GC37, and GC27, including the SST record from GeoB7926-2 plotted on a reversed axis [*Romero et al.*, 2008]. (b) The gradient (difference) in opal flux between three cores and GC68. The distance between cores (in degrees latitude) is noted next to each pair of cores.

peaks in opal and C_{org} fluxes, and core GC49 shows increased C_{org} fluxes and opal fluxes relative to the late Holocene. All three cores are near the region of maximum modern upwelling, and the HS1 peaks represent fluxes 50% greater than late Holocene values. Foraminiferal and diatom assemblages from nearby cores indicate increased upwelling (and upwelling-derived productivity) during HS1, and bulk geochemical data also suggest increased biogenic fluxes to the sediment [*Mulitza et al.*, 2008; *Romero et al.*, 2008; *Zarriess and Mackensen*, 2010]. Alkenone-based SST reconstructions during HS1 show the lowest temperatures over the last 25 kyr with the exception of the YD [*Romero et al.*, 2008]. Dust fluxes to the sediment in this region were also greater during HS1 [*Adkins et al.*, 2006; *Jullien et al.*, 2007; *Just et al.*, 2012; *McGee et al.*, 2013]. Increased dust and biogenic sediment fluxes and decreased SSTs along the northwest African margin during HS1 occurred in association with

widespread evidence for drying in tropical and subtropical Africa [*Stager et al*., 2011] and a southward shift of the Atlantic ITCZ and Sahel-Sahara boundary [*Collins et al*., 2013; *Peterson et al*., 2000].

During the Younger Dryas we observe increased opal fluxes in cores GC37, GC49, and GC68 and elevated C_{org} fluxes relative to coretop values in the same three cores. This increase in biogenic sedimentation is also found in nearby core ODP 658C [*Adkins et al*., 2006] and is consistent with nearby data suggesting an increase in upwelling-derived biological productivity [*Romero et al*., 2008]. Decreased SSTs (see Figure 3a [*Romero et al*., 2008; *Zhao et al*., 1995; *Zhao et al*., 2000]) are also observed at this time. This increase in upwelling again occurs in association with increased dust fluxes [*Adkins et al*., 2006; *McGee et al*., 2013] and hydrological evidence of a weakening of the West African monsoon such as reduced river discharge [*Weldeab et al*., 2007].

The HS1 and YD cooling events are thus each marked by increased biogenic sedimentation, decreased SSTs, and increased dust fluxes. Individually, each of these changes can be difficult to interpret, and none requires increased surface winds on its own. Increased biogenic fluxes can result from increases in the nutrient content of upwelled waters rather than increased upwelling, as discussed in section 5.3. Decreased SSTs during millennial-scale events may result from an increase in the advection of cool North Atlantic waters via the Canary current [*deMenocal et al*., 2000a; *Zhao et al*., 1995]. Likewise, dust flux increases may result from decreases in source area precipitation and vegetation [e.g., *Rea*, 1994; *Mahowald et al*., 2006] rather than increased wind strength.

Taken together, however, the strongly correlated increases in productivity and dust deposition and decreases in SSTs during millennial-scale cooling events are best explained by a common driver: strengthened northeasterly surface winds. Modern climate data (section 2) suggest that this covariability is most likely related to a strengthening and/or southward displacement of the Atlantic subtropical high in winter and spring in association with a southward displacement of the Atlantic ITCZ, leading to stronger northeasterly trade winds along the margin. Our data suggest that this trade wind intensification extended at least from 19 to 27°N, with greatest intensification at the southern end of this transect.

Beyond being the most parsimonious interpretation of the data, this conclusion is also supported by modern observations and model results highlighting the sensitivity of dust fluxes and upwelling to wind strength (section 2.2). High-speed wind events ("gustiness" as described by *McGee et al*. [2010]) are of particular importance due to the nonlinear dependence of both dust emissions and upwelling to wind speed. Modern data show a strong correlation between gustiness and dust emissions, both globally [*Engelstaedter and Washington*, 2007b] and in North Africa [*Engelstaedter and Washington*, 2007a; *Todd et al*., 2007]. While upwelling is usually discussed in terms of wind strength, gustiness plays an important role here as well. Since surface Ekman transport is directly proportional to wind stress, and wind stress is roughly proportional to the square of wind speed, strong winds have a much larger effect on upwelling. Furthermore, ecological modeling has shown that ideal conditions for biological productivity result not from sustained strong winds but from periodic increases in wind speed interspersed with periods of relaxation [*Yokomizo et al*., 2010]. We therefore interpret the concurrent increases in opal, C_{org}, and dust fluxes, and decreases in SSTs to be consistent with strengthened trade wind-driven upwelling during HS1 and the YD.

Trade wind intensification during HS1 and the YD provides important confirmation of model simulations of North Atlantic cooling events. Cooling at higher latitudes drives advection of anomalously cold, dry air by the climatological winds, leading to increased surface pressure in the North Atlantic subtropical high and over the continent [*Liu et al*., 2014; *Zhang and Delworth*, 2005]; these pressure changes increase northeasterly wind strength both along the coast and over central North Africa. A separate North Atlantic cooling simulation that included prognostic dust emissions found that the southward shift of the ITCZ coupled with wind strength played a leading role in increasing dust mobilization and transport, while aridity played a minor role in increasing dust fluxes in northwest Africa [*Murphy et al*., 2014]. Importantly, these anomalous near-surface northeasterly winds appear to be a primary driver of drying in the Sahel in response to North Atlantic cooling, as they advect low-moist static energy air from higher latitudes. The resulting "ventilation" of the monsoon region causes a reduction of summer monsoon strength and a southward shift of monsoon precipitation [*Liu et al*., 2014].

5.2. The African Humid Period

The three cores between 19 and 27°N show results consistent with significantly decreased wind strength during the African Humid Period. Cores GC37, GC49, and GC68 all exhibit minima in opal and C_{org} fluxes during

this time. Decreased paleoproductivity during the AHP is also documented at numerous nearby sites [*Adkins et al*., 2006; *deMenocal et al*., 2000a, 2000b; *Romero et al*., 2008; *Zarriess and Mackensen*, 2010]. Alkenone data indicate increased SSTs at and near ODP658C during the AHP [*Romero et al*., 2008; *Zhao et al*., 1995; *Zhao et al*., 2000], again consistent with decreased upwelling intensity.

Previously published data from cores GC37, GC49, and GC68 and from ODP658C show that the AHP is also marked by dust flux minima [*Adkins et al*., 2006; *McGee et al*., 2013]. As in the discussion of millennial-scale cold events above (section 5.1), the correspondence between biogenic sediment fluxes, SSTs, and dust fluxes is most easily explained by a change in surface wind strength. Dust fluxes may have been further reduced by changes in source area aridity, as lake level and pollen evidence indicates that soil moisture and vegetation density were significantly higher in the Sahara and Sahel during the AHP [e.g., *Bartlein et al*., 2011; *Hoelzmann et al*., 1998]. However, even under the higher precipitation rates of the AHP, it is likely that wind strength would have been a primary determinant of dune activity and thus coarse-grained dust emissions [*Roskin et al*., 2011; *Tsoar*, 2005].

The collapse of biogenic and dust fluxes and rise in SSTs during the AHP thus points to a dramatic reduction of winter northeasterly trade winds. Modern winter wind variability along the margin tracks the strength of the North Atlantic subtropical high (section 2.2). During the AHP, weaker winter winds may have resulted from a weakening or northward displacement of this high. Most modeling and data-based studies suggest a stronger subtropical high (more positive NAO) during the early Holocene [e.g., *Gladstone et al*., 2005; *Mauri et al*., 2014; *Wanner et al*., 2008]. *Walczak et al*. [2015] conclude based on a compilation of paleoclimate data from western Europe that the subtropical high was located substantially farther north during the early Holocene and that the high has shifted south during the middle to late Holocene. Our data suggest that if the high was not weaker in the early Holocene, its northward displacement was large enough to substantially reduce northeasterly wind strength along the northwest African margin.

Modeling studies simulating the response of North African climate to orbital precession suggest that the strengthening of the West African summer monsoon is accompanied by westerly (on-land) wind anomalies that advect moisture into the central Sahara [*Battisti et al*., 2014; *Patricola and Cook*, 2007]. Though these models focus on the wind response during boreal summer, they also suggest that northeasterly winds are reduced along at least the southern portion of our transect in response to stronger summer insolation.

Although the precessional forcing of the termination of the AHP was gradual, several studies have shown that the climate response during this transition was abrupt. Opal and dust fluxes in core ODP 658C show abrupt, synchronous increases at the termination of the AHP [*Adkins et al*., 2006; *deMenocal et al*., 2000b]. A sea surface salinity reconstruction in the Gulf of Guinea reflecting Niger River discharge shows a similarly abrupt transition, suggesting that changes in total precipitation and river runoff in the core of the rain belt occurred rapidly [*Weldeab et al*., 2007]. A persistent question has been whether or not these abrupt changes show any systematic difference in timing with latitude, as might be predicted from the gradual change in the latitude of maximum summer insolation over time. *McGee et al*. [2013] addressed this question using bioturbation modeling to determine the timing of the transitions into and out of the AHP using the same cores presented here. They showed that the transition out of the AHP is consistent with simultaneous, abrupt changes in dust flux between 19°N and 27°N. This suggests that vegetation-albedo feedbacks and sea surface temperature moisture feedbacks [*Claussen et al*., 1999; *deMenocal et al*., 2000b] were operating rapidly on relatively large spatial scales; our data suggest that these abrupt transitions affected surface trade wind strength in addition to precipitation. In the central and eastern Sahara there is evidence for more gradual transitions out of the humid period between 3 and 7 ka [*Kropelin et al*., 2008; *Weldeab et al*., 2014], whereas for the Horn of Africa and East Africa the transition appears to be abrupt near 5 ka [*Tierney and deMenocal*, 2013]. A recent compilation of African hydrologic reconstructions by *Shanahan et al*. [2015] suggests that, while local decreases in precipitation were abrupt at the end of the AHP, the location of these local decreases occurred first in the north and moved gradually southward over time. While the age models of all four cores do not enable us to confirm this spatial trend, our data show that in the region of maximum modern upwelling (e.g., core GC68) increased opal and C_{org} fluxes were abrupt and simultaneous with increased dust fluxes. This suggests that in addition to the abrupt hydrologic responses outlined by Shanahan and coauthors, there was an abrupt strengthening of northeasterly winds in the area of maximum modern upwelling at ~5 ka.

5.3. Influences of Upwelling Strength and Water Nutrient Content on Biogenic Fluxes

Opal (and C_{org}) fluxes in this region are strongly influenced by the strength of trade wind-driven upwelling [*Adkins et al*., 2006], with additional contributions from changes in the nutrient content of upwelled water masses [*Romero et al*., 2008]. Paleodust fluxes have also been shown to be strongly influenced by wind strength and gustiness and to correlate with the position of the ITCZ [*McGee et al*., 2010; *Murphy et al*., 2014], with an uncertain contribution from changes in precipitation and vegetation in the Sahara. This study is unique in that it combines ^{230}Th normalization and biogenic fluxes with previously published dust fluxes in the same north-south transect of cores. As such, we can directly compare eolian and biogenic fluxes from the same samples and compare how fluxes change along the margin. While both biogenic and dust fluxes are each affected by multiple drivers, they have one primary driver in common: wind strength and gustiness, as primarily determined by the strength and position of the ITCZ. Therefore, when biogenic fluxes and dust fluxes change with similar magnitude and timing, as they do in our cores, we suggest that changes in wind strength are a major driver of these changes, with precipitation and ocean nutrients playing a smaller role.

To gain a first-order understanding of changes in nutrient supply along the margin, we look at the ratio of opal flux to $CaCO_3$ flux (Figure 3a). While acknowledging that both burial flux indicators are altered by unknown loss terms due to remineralization and preservation, the broad trends may be used to examine the causes of the observed biogenic flux changes. The ratio of opal to carbonate is a nonquantitative indicator of the degree to which diatoms outcompete coccolithophorids for nutrients, and it is particularly useful in distinguishing periods of relatively high (or low) opal flux from periods when all biogenic fluxes increase or decrease more uniformly. Diatoms compete more effectively for other nutrients in areas with increased Si:N ratios in the upwelled water, such as the Southern Ocean, and in nutrient-rich coastal upwelling zones such as the African margin [*Egge and Aksnes*, 1992; *Ragueneau et al*., 2000]. Therefore, higher opal:$CaCO_3$ ratios are usually interpreted as an indication of increased Si supply, whether in total or relative to N, and may be interpreted as an indication of the increased importance of seasonal upwelling blooms to overall biogenic export.

To differentiate between the effects of increased upwelling strength and changes in the nutrient content of upwelled water, we can compare changes in opal:$CaCO_3$ over time with the alkenone-based SST record from nearby core GeoB7926-2 (Figure 3a) [*Romero et al*., 2008]. We observe that high opal:$CaCO_3$ ratios during HS1 and the YD are accompanied by low SSTs and that low opal:$CaCO_3$ ratios during the AHP coincide with the period of highest SSTs throughout the record. When considered alongside evidence for increased dust fluxes during HS1 and the YD and decreased dust fluxes during the AHP [*Adkins et al*., 2006; *Jullien et al*., 2007; *McGee et al*., 2013; *Tjallingii et al*., 2008; *Zarriess and Mackensen*, 2010], these data suggest that changes in the strength of upwelling were a strong driver of the observed changes in primary productivity. We suggest that while changes in productivity may have been secondarily affected by changes in the nutrient context of upwelled water, these changes were either covarying (increased nutrient content with increased upwelling and vice versa) or not large enough in the opposite direction to make a difference.

We cannot rule out the possibility of changes in upwelled nutrient concentration, however, particularly if changes in water mass formation and therefore nutrient content are linked to the same changes in atmospheric circulation responsible for strengthened trade winds. Previous work suggests increased export of Si-rich southern-sourced intermediate waters during HS1 and the YD due to a southward shift in the Southern Hemisphere Westerlies and increased overturning in the Southern Ocean during these events [*Anderson et al*., 2009; *Hendry et al*., 2012]. Indeed, silicic acid concentrations reconstructed from the silicon isotopic composition of sponge spicules suggest increased Si availability at 1400 m water depth in the western midlatitude Atlantic during HS1 [*Hendry et al*., 2014], as well as elevated Si concentrations during HS1 and the YD at 1000 m in the midlatitude south Atlantic [*Hendry et al*., 2012]. The magnitude of the changes is somewhat larger in the South Atlantic, particularly during the YD, consistent with the interpretation that the nutrients originated in the Southern Ocean. A silicon isotope record from the African margin would be a valuable contribution to the literature as it would further clarify the role of changing silicic acid concentration on diatom productivity through time.

Alternatively, *Romero et al*. [2008] suggest that the slowdown in Atlantic meridional overturning circulation during HS1 may have caused the Canary Current to detach from the shelf farther north, allowing the upwelling of relatively nutrient-rich SACW over a greater area than today. Romero and coauthors do not rule out the possibility that intensified trade winds resulted in stronger upwelling overall, and SST in the Romero record

decreases simultaneously with an increase in opal % and the number of diatom valves per gram, suggesting a strong upwelling component. *Meckler et al.* [2013] observe peaks in Si/Al ratios in ODP 658 during glacial terminations over the past ~600 ka. They interpret these data as evidence that a decrease in the production of glacial North Atlantic intermediate water allowed upward mixing of Si-rich southern-sourced deep water during these transitions. Finally, *Gallego-Torres et al.* [2014] observe increased Mo/Al and U/Al ratios at 2500 m water depth on the African Margin during HS1 and the YD. They interpret these redox-sensitive metals as evidence for oxygen depletion as the result of reduced North Atlantic Deep Water formation and subsequently reduced ventilation at the core site, in combination with increased surface productivity. Therefore, while the covariation of opal and C_{org} with dust fluxes in our cores suggests a strong wind-driven upwelling component, we cannot rule out the possibility that increased biogenic fluxes during HS1 and the YD reflect a combination of changes in wind strength and nutrient supply, which is in turn partially driven by both local and remote changes in ocean circulation.

5.4. Meridional Opal Flux Gradient Changes

We can utilize the large latitudinal range of these cores to examine changes in the north-south gradient of opal flux over time. This gradient can be interpreted as a nonquantitative proxy for the relative strength of upwelling along the margin over time and can help to constrain the timing and magnitude of latitudinal changes in wind strength. Because the four cores are sampled at different temporal resolutions, opal data were interpolated and resampled every 1 ka using the piecewise linear integration interpolation in AnalySeries 2.0 [*Paillard et al.*, 1996]. We then calculated the difference between each core and core GC68, the core with the highest opal fluxes, at each time point (Figure 3b). In order to ensure that differences were not simply due to the increased relative importance of bioturbation in cores with lower sedimentation rates, we ran the same analysis with bins of 1.5 ka, 2 ka, and 3 ka (not shown). While the absolute values of the difference in flux between cores changed (as expected), the general latitudinal trends over time did not.

We observe two general patterns. First, the gradients (differences) between GC68 and the three other cores all increase during HS1 and the YD and show minima during the AHP. Second, the magnitude of the increased gradients during HS1 and the YD scales with the difference in latitude between the two cores. In other words, during the YD the difference in opal flux between southernmost site GC68 (19°N) and northernmost site GC27 (31°N) is greater than the difference between GC68 (19°N) and GC37 (27°N), which is greater than the difference between GC68 (19°N) and GC49 (23°N). Both observations are consistent with a southward shift in the area of strongest trade winds during HS1 and the YD, which would have increased upwelling at southern sites relatively more than northern ones. This is also consistent with previous work reconstructing the upwelling filament position and geometry during abrupt cooling events. A paleoproductivity reconstruction from 20°N (between southernmost cores GC68 and GC49) has been interpreted as evidence for a larger filament positioned farther from shore, greatly increasing diatom flux to the seafloor and also the abundance of upwelling-favorable taxa [*Romero et al.*, 2008]. Farther north, a record from Cape Yubi (27°N, between cores GC27 and GC37) shows evidence for increased upwelling due to the position of the ITCZ during abrupt cooling events but not evidence for the intense filament formation inferred farther south [*Holzwarth et al.*, 2010]. This likely explains why, even though we see increased opal and C_{org} fluxes in all cores during the YD (Figure 2), the flux gradient between northern and southern cores is also greatest at this time.

In contrast to periods of abrupt climate change, the gradients between our four cores are consistent with a weakening of the trade winds during the AHP but not necessarily a northward shift in the area of strongest upwelling. Rather, we see that the difference in opal flux between the northernmost core and the southernmost core reach zero at this time as opal fluxes in all cores decrease to minimum values. The northernmost core (GC27; 31°N) is in a region of low modern upwelling, while the southernmost core (GC68; 19°N) is in an area of strong winter and spring upwelling [*Mittelstaedt*, 1991]. The lack of a strong north-south productivity gradient along the margin at these latitudes is consistent with much of what is known about atmospheric circulation during the AHP, when modeling results suggest that meridional winds and upwelling strength were reduced during all seasons along the northwest African margin [*Liu et al.*, 2007]. Our data show that this change in trade wind strength significantly reduced upwelling-derived productivity along nearly the entire northwest African margin during the AHP, extending from south of Cape Blanc throughout the area of maximum and continuous modern upwelling to the north. This is consistent with weakened offshore spreading of the upwelling filament [*Romero et al.*, 2008], even as the length of the filament gradually increased to the

North throughout the later portion of the AHP due to a combination of sea level rise (and its effect on coastal morphology) and movement of the trade winds [*Holzwarth et al*., 2010].

Lastly, our combined dust and opal flux data can be used to constrain the paleoclimatic origin of gradual or abrupt sediment flux changes in these northwest African cores. The close correlation between eolian and paleoproductivity flux proxies within and between all cores suggests a common physical mechanism—trade wind speed and orientation. While each core records consistent changes in these proxies throughout the deglacial sequence, the synchronous shifts between the mineral eolian fluxes and the biogenic opal and Corg fluxes are best explained by changes in the direction or competence of surface trade winds [*Engelstaedter and Washington*, 2007b; *McGee et al*., 2010, 2013]. This would apply to evidence for both abrupt and gradual paleoclimate changes in cores with sedimentation rates high enough to overcoming smoothing effects due to bioturbation [*McGee et al*., 2013].

6. Conclusion

Opal and C_{org} fluxes in a transect of four cores along the northwest African margin show synchronous changes during both abrupt and orbitally forced climatic events. Decreased biogenic fluxes in all cores during the AHP are consistent with reduced wind-driven upwelling due to weakened trade winds and a northward shift in the ITCZ. The collapse of the gradient in opal flux between cores suggests that rather than a northward shift in the area of maximum upwelling, however, the entire margin between at least 19°N and 27°N experienced reduced upwelling. Decreased dust fluxes in the same cores during the AHP [*McGee et al*., 2013] support the conclusion that wind strength was indeed reduced along the entire transect at this time.

We observe peaks in opal flux during HS1 and the YD in cores GC68 and GC37 and a peak in both opal and C_{org} fluxes during the YD in core GC49. The peaks in biogenic fluxes in each core are coincident with peaks in dust flux of similar relative magnitude [*McGee et al*., 2013]; these peaks also occur simultaneously with SST minima observed in a nearby core [*Romero et al*., 2008]. The maximum latitudinal gradients in opal flux occur during HS1 and the YD, as the southern cores experienced relatively greater increases in opal flux than cores farther to the north. These data provide strong support for a strengthening and a southward shift in the position of the trade winds during periods of abrupt cooling in the North Atlantic, which would have increased wind-driven upwelling along much of the coast but increased upwelling at southern sites relatively more than northern ones. This is consistent with models that show increased northeasterly winds between 15 and 25°N along the African Margin during abrupt North Atlantic coolings [*Liu et al*., 2014].

Our data add to a growing body of evidence that shows that the African monsoon and associated coastal upwelling system are highly sensitive to both gradual changes in orbital forcing and abrupt climate change in the North Atlantic. The African margin continues to provide an excellent archive for terrigenous and biogenic proxies alike and is a valuable resource in reconstructing changes in this complex climate regime. These results and others may also serve as the basis for testing and improving the atmospheric response to both orbital forcing and abrupt North Atlantic cooling in global and regional climate models.

Acknowledgments

The authors thank J. Thole at Macalester College and P. Malone at LDEO for their laboratory assistance. This paper is dedicated to the memory of Pat Malone and her generous help with students, postdocs, and scientists. This work was funded by NSF grants OCE-1103262 (L. Bradtmiller), OCE-1030784 (D. McGee and P. deMenocal), and OCE-0402348 (P. deMenocal) and the Center for Climate and Life at Lamont-Doherty Earth Observatory of Columbia University. Data used in this paper can be found at the NOAA National Climatic Data Center (http://www.ncdc.noaa.gov/).

References

Abrantes, F. (2000), 200 000 yr diatom records from Atlantic upwelling sites reveal maximum productivity during LGM and a shift in phytoplankton community structure at 185 000 yr, *Earth Planet. Sci. Lett.*, *176*(1), 7–16.

Adkins, J., P. Demenocal, and G. Eshel (2006), The "African humid period" and the record of marine upwelling from excess Th-230 in Ocean Drilling Program Hole 658C, *Paleoceanography*, *21*, PA4203, doi:10.1029/2005PA001200.

Anderson, R. F., and A. P. Fleer (1982), Determination of natural actinides and plutonium in marine particulate material, *Anal. Chem.*, *54*(7), 1142–1147.

Anderson, R. F., M. P. Bacon, and P. G. Brewer (1983), Removal of Th-230 and Pa-231 from the open ocean, *Earth Planet. Sci. Lett.*, *62*(1), 7–23.

Anderson, R. F., Y. Lao, W. S. Broecker, S. E. Trumbore, H. J. Hofmann, and W. Wolfli (1990), Boundary scavenging in the Pacific Ocean—A comparison of Be-10 and Pa-231, *Earth Planet. Sci. Lett.*, *96*(3–4), 287–304.

Anderson, R. F., S. Ali, L. I. Bradtmiller, S. H. H. Nielsen, M. Q. Fleisher, B. E. Anderson, and L. H. Burckle (2009), Wind-driven upwelling in the Southern Ocean and the deglacial rise in atmospheric CO_2, *Science*, *323*(5920), 1443–1448.

Bakun, A. (1990), Global climate change and intensification of coastal ocean upwelling, *Science*, *247*(4939), 198–201.

Bard, E. (2002), Climate shock: Abrupt changes, over millennial time scales, *Phys. Today*, *55*(12), 32–38.

Bard, E., M. Arnold, J. Mangerud, M. Paterne, L. Labeyrie, J. Duprat, M. A. Melieres, E. Sonstegaard, and J. C. Duplessy (1994), The North Atlantic atmosphere-sea surface C-14 gradient during the Younger Dryas climatic event, *Earth Planet. Sci. Lett.*, *126*(4), 275–287.

Bartlein, P. J., et al. (2011), Pollen-based continental climate reconstructions at 6 and 21 ka: A global synthesis, *Clim. Dyn.*, *37*(3–4), 775–802.

Battisti, D. S., Q. H. Ding, and G. H. Roe (2014), Coherent pan-Asian climatic and isotopic response to orbital forcing of tropical insolation, *J. Geophys. Res. Atmos.*, *119*, 11,997–12,020, doi:10.1002/2014JD021960.

Berger, A., and M. F. Loutre (1991), Insolation values for the climate of the last 10000000 years, *Quat. Sci. Rev.*, *10*(4), 297–317.
Bertrand, P., et al. (1996), The glacial ocean productivity hypothesis: The importance of regional temporal and spatial studies, *Mar. Geol.*, *130*(1–2), 1–9.
Bory, A. J. M., and P. P. Newton (2000), Transport of airborne lithogenic material down through the water column in two contrasting regions of the eastern subtropical North Atlantic Ocean, *Global Biogeochem. Cycles*, *14*(1), 297–315, doi:10.1029/1999GB900098.
Boyd, P. W., and T. W. Trull (2007), Understanding the export of biogenic particles in oceanic waters: Is there consensus?, *Prog. Oceanogr.*, *72*(4), 276–312.
Bradtmiller, L. I., R. F. Anderson, M. Q. Fleisher, and L. H. Burckle (2007), Opal burial in the equatorial Atlantic Ocean over the last 30kyr: Implications for glacial-interglacial changes in the ocean silicon cycle, *Paleoceanography*, *22*, PA4216, doi:10.1029/2007PA001443.
Broccoli, A. J., K. A. Dahl, and R. J. Stouffer (2006), Response of the ITCZ to Northern Hemisphere cooling, *Geophys. Res. Lett.*, *33*, L01702, doi:10.1029/2005GL024546.
Bronk Ramsey, C. (2009), Bayesian analysis of radiocarbon dates, *Radiocarbon*, *51*(1), 337–360.
Buesseler, K. O. (1998), The decoupling of production and particulate export in the surface ocean, *Global Biogeochem. Cycles*, *12*(2), 297–310, doi:10.1029/97GB03366.
Buesseler, K. O., et al. (2007), Revisiting carbon flux through the ocean's twilight zone, *Science*, *316*(5824), 567–570.
Chapman, M. R., N. J. Shackleton, and J. C. Duplessy (2000), Sea surface temperature variability during the last glacial-interglacial cycle: Assessing the magnitude and pattern of climate change in the North Atlantic, *Palaeogeogr. Palaeoclimatol. Palaeoecol.*, *157*(1–2), 1–25.
Chiapello, I., C. Moulin, and J. M. Prospero (2005), Understanding the long-term variability of African dust transport across the Atlantic as recorded in both Barbados surface concentrations and large-scale Total Ozone Mapping Spectrometer (TOMS) optical thickness, *J. Geophys. Res.*, *110*, D18S10, doi:10.1029/2004JD005132.
Claussen, M., C. Kubatzki, V. Brovkin, A. Ganopolski, P. Hoelzmann, and H. J. Pachur (1999), Simulation of an abrupt change in Saharan vegetation in the mid-Holocene, *Geophys. Res. Lett.*, *26*(14), 2037–2040, doi:10.1029/1999GL900494.
Claussen, M., A. Ganopolski, V. Brovkin, F. W. Gerstengarbe, and P. Werner (2003), Simulated global-scale response of the climate system to Dansgaard/Oeschger and Heinrich events, *Clim. Dyn.*, *21*(5–6), 361–370.
Collins, J. A., A. Govin, S. Mulitza, D. Heslop, M. Zabel, J. Hartmann, U. Rohl, and G. Wefer (2013), Abrupt shifts of the Sahara-Sahel boundary during Heinrich stadials, *Clim. Past*, *9*(3), 1181–1191.
Cropper, T. E., E. Hanna, and G. R. Bigg (2014), Spatial and temporal seasonal trends in coastal upwelling off Northwest Africa, 1981–2012, *Deep Sea Res., Part I*, *86*, 94–111.
deMenocal, P. B., J. Ortiz, T. Guilderson, and M. Sarnthein (2000a), Coherent high- and low-latitude climate variability during the Holocene warm period, *Science*, *288*(5474), 2198–2202.
deMenocal, P. B., J. Ortiz, T. Guilderson, J. Adkins, M. Sarnthein, L. Baker, and M. Yarusinsky (2000b), Abrupt onset and termination of the African Humid Period: Rapid climate responses to gradual insolation forcing, *Quat. Sci. Rev.*, *19*(1–5), 347–361.
Doherty, O. M., N. Riemer, and S. Hameed (2012), Control of Saharan mineral dust transport to Barbados in winter by the Intertropical Convergence Zone over West Africa, *J. Geophys. Res.*, *117*, D19117, doi:10.1029/2012JD017767.
Egge, J. K., and D. L. Aksnes (1992), Silicate as regulating nutrient in phytoplankton competition, *Mar. Ecol. Prog. Ser.*, *83*(2–3), 281–289.
Engelstaedter, S., and R. Washington (2007a), Atmospheric controls on the annual cycle of North African dust, *J. Geophys. Res.*, *112*, D03103, doi:10.1029/2006JD007195.
Engelstaedter, S., and R. Washington (2007b), Temporal controls on global dust emissions: The role of surface gustiness, *Geophys. Res. Lett.*, *34*, L15805, doi:10.1029/2007GL029971.
Evan, A. T., C. Flamant, C. Lavaysse, C. Kocha, and A. Saci (2015), Water vapor-forced greenhouse warming over the Sahara Desert and the recent recovery from the Sahelian drought, *J. Clim.*, *28*(1), 108–123.
Fischer, G., and G. Karakaş (2009), Sinking rates and ballast composition of particles in the Atlantic Ocean: Implications for the organic carbon fluxes to the deep ocean, *Biogeosciences*, *6*(1), 85–102.
Fleisher, M. Q., and R. F. Anderson (2003), Assessing the collection efficiency of Ross Sea sediment traps using Th-230 and Pa-231, *Deep Sea Res., Part II*, *50*(3–4), 693–712.
Francois, R., S. Honjo, R. Krishfield, and S. Manganini (2002), Factors controlling the flux of organic carbon to the bathypelagic zone of the ocean, *Global Biogeochem. Cycles*, *16*(4), 1087, doi:10.1029/2001GB001722.
Freudenthal, T., H. Meggers, J. Henderiks, H. Kuhlmann, A. Moreno, and G. Wefer (2002), Upwelling intensity and filament activity off Morocco during the last 250,000 years, *Deep Sea Res., Part II*, *49*(17), 3655–3674.
Fütterer, D. K. (1983), The modern upwelling record off northwest Africa, in *Coastal Upwelling, Its Sediment Record. Part B: Sedimentary Records of Ancient Coastal Upwelling*, edited by J. Thiede and E. Suess, pp. 105–121, Plenum, New York.
Gallego-Torres, D., O. E. Romero, F. Martinez-Ruiz, J. H. Kim, B. Donner, and M. Ortega-Huertas (2014), Rapid bottom-water circulation changes during the last glacial cycle in the coastal low-latitude NE Atlantic, *Quat. Res.*, *81*(2), 330–338.
Garcia, H. E., R. A. Locarnini, T. P. Boyer, J. I. Antonov, M. M. Zweng, O. K. Baranova, and D. R. Johnson (2010), *World Ocean Atlas 2009, Volume 4: Nutrients (Phosphate, Nitrate, Silicate)*, *NOAA Atlas NESDIS*, vol. 71, edited by S. Levitus, 398 pp., U.S. Gov. Print. Off., Washington, D. C.
Gasse, F. (2000), Hydrological changes in the African tropics since the Last Glacial Maximum, *Quat. Sci. Rev.*, *19*(1–5), 189–211.
Gasse, F., R. Tehet, A. Durand, E. Gibert, and J. C. Fontes (1990), The arid-humid transition in the Sahara and the Sahel during the last deglaciation, *Nature*, *346*(6280), 141–146.
Gil, I. M., F. Abrantes, and D. Hebbeln (2007), Diatoms as upwelling and river discharge indicators along the Portuguese margin: Instrumental data linked to proxy information, *Holocene*, *17*(8), 1245–1252.
Gladstone, R. M., et al. (2005), Mid-Holocene NAO: A PMIP2 model intercomparison, *Geophys. Res. Lett.*, *32*, L16707, doi:10.1029/2005GL023596.
Guidi, L., L. Stemmann, G. A. Jackson, F. Ibanez, H. Claustre, L. Legendre, M. Picheral, and G. Gorsky (2009), Effects of phytoplankton community on production, size and export of large aggregates: A world-ocean analysis, *Limnol. Oceanogr.*, *54*(6), 1951–1963.
Helmke, P., O. Romero, and G. Fischer (2005), Northwest African upwelling and its effect on offshore organic carbon export to the deep sea, *Global Biogeochem. Cycles*, *19*, GB4015, doi:10.1029/2004GB002265.
Henderson, G. M., C. Heinze, R. F. Anderson, and A. M. E. Winguth (1999), Global distribution of the Th-230 flux to ocean sediments constrained by GCM modelling, *Deep Sea Res., Part I*, *46*(11), 1861–1893.
Hendry, K. R., L. F. Robinson, M. P. Meredith, S. Mulitza, C. M. Chiessi, and H. Arz (2012), Abrupt changes in high-latitude nutrient supply to the Atlantic during the last glacial cycle, *Geology*, *40*(2), 123–126.
Hendry, K. R., L. F. Robinson, J. F. McManus, and J. D. Hays (2014), Silicon isotopes indicate enhanced carbon export efficiency in the North Atlantic during deglaciation, *Nat. Commun.*, *5*, 3107, doi:10.1038/ncomms4107.

Hoelzmann, P., D. Jolly, S. P. Harrison, F. Laarif, R. Bonnefille, and H. J. Pachur (1998), Mid-Holocene land-surface conditions in northern Africa and the Arabian Peninsula: A data set for the analysis of biogeophysical feedbacks in the climate system, *Global Biogeochem. Cycles*, *12*(1), 35–51, doi:10.1029/97GB02733.

Hoelzmann, P., F. Gasse, L. M. Dupont, U. Salzmann, M. Staubwasser, D. C. Leuchner, and F. Sirocko (2004), Palaeoenvironmental changes in the aird and subarid belt (Sahara-Sahel-Arabian Peninsula) from 150 ka to the present, in *Past Climate through Europe and Africa*, edited by R. W. Battarbee, F. Gasse, and C. S. Stickley, pp. 219–256, Springer, Dordrecht.

Holzwarth, U., H. Meggers, O. Esper, H. Kuhlmann, T. Freudenthal, C. Hensen, and K. A. F. Zonneveld (2010), NW African climate variations during the last 47,000 years: Evidence from organic-walled dinoflagellate cysts, *Palaeogeogr. Palaeoclimatol. Palaeoecol.*, *291*(3–4), 443–455.

Honda, M. C., and S. Watanabe (2010), Importance of biogenic opal as ballast of particulate organic carbon (POC) transport and existence of mineral ballast-associated and residual POC in the Western Pacific Subarctic Gyre, *Geophys. Res. Lett.*, *37*, L02605, doi:10.1029/2009GL041521.

Jullien, E., et al. (2007), Low-latitude "dusty events" vs. high-latitude "icy Heinrich events", *Quat. Res.*, *68*(3), 379–386.

Just, J., D. Heslop, T. von Dobeneck, T. Bickert, M. J. Dekkers, T. Frederichs, I. Meyer, and M. Zabel (2012), Multiproxy characterization and budgeting of terrigenous end-members at the NW African continental margin, *Geochem. Geophys. Geosyst.*, *13*, Q0AO01, doi:10.1029/2012GC004148.

Klaas, C., and D. E. Archer (2002), Association of sinking organic matter with various types of mineral ballast in the deep sea: Implications for the rain ratio, *Global Biogeochem. Cycles*, *16*(4), 1116, doi:10.1029/2001GB001765.

Koning, E., J. M. van Iperen, W. van Raaphorst, W. Helder, G. J. A. Brummer, and T. C. E. van Weering (2001), Selective preservation of upwelling-indicating diatoms in sediments off Somalia, NW Indian Ocean, *Deep Sea Res., Part I*, *48*(11), 2473–2495.

Kropelin, S., et al. (2008), Climate-driven ecosystem succession in the Sahara: The past 6000 years, *Science*, *320*(5877), 765–768.

Kuhlmann, H., H. Meggers, T. Freudenthal, and G. Wefer (2004a), The transition of the monsoonal and the N Atlantic climate system off NW Africa during the Holocene, *Geophys. Res. Lett.*, *31*, L22204, doi:10.1029/2004GL021267.

Kuhlmann, H., T. Freudenthal, P. Helmke, and H. Meggers (2004b), Reconstruction of paleoceanography off NW Africa during the last 40,000 years: Influence of local and regional factors on sediment accumulation, *Mar. Geol.*, *207*(1–4), 209–224.

Kuper, R., and S. Kropelin (2006), Climate-controlled Holocene occupation in the Sahara: Motor of Africa's evolution, *Science*, *313*(5788), 803–807.

Liu, Y. W., J. C. H. Chiang, C. Chou, and C. M. Patricola (2014), Atmospheric teleconnection mechanisms of extratropical North Atlantic SST influence on Sahel rainfall, *Clim. Dyn.*, *43*(9–10), 2797–2811.

Liu, Z., et al. (2007), Simulating the transient evolution and abrupt change of Northern Africa atmosphere–ocean-terrestrial ecosystem in the Holocene, *Quat. Sci. Rev.*, *26*(13–14), 1818–1837.

Locarnini, R. A., A. V. Mishonov, J. I. Antonov, T. P. Boyer, H. E. Garcia, O. K. Baranova, M. M. Zweng, and D. R. Johnson (2010), in *World Ocean Atlas 2009, Volume 1: Temperature*, *NOAA Atlas NESDIS*, vol. 68, edited by S. Levitus, 184 pp., U.S. Gov. Print. Off., Washington, D. C.

Mahowald, N. M., D. R. Muhs, S. Levis, P. J. Rasch, M. Yoshioka, C. S. Zender, and C. Luo (2006), Change in atmospheric mineral aerosols in response to climate: Last glacial period, preindustrial, modern, and doubled carbon dioxide climates, *J. Geophys. Res.*, *111*, D10202, doi:10.1029/2005JD006653.

Manning, K., and A. Timpson (2014), The demographic response to Holocene climate change in the Sahara, *Quat. Sci. Rev.*, *101*, 28–35.

Martinez, P., P. Bertrand, G. B. Shimmield, K. Cochrane, F. J. Jorissen, J. Foster, and M. Dignan (1999), Upwelling intensity and ocean productivity changes off Cape Blanc (northwest Africa) during the last 70,000 years: Geochemical and micropalaeontological evidence, *Mar. Geol.*, *158*(1–4), 57–74.

Mauri, A., B. A. S. Davis, P. M. Collins, and J. O. Kaplan (2014), The influence of atmospheric circulation on the mid-Holocene climate of Europe: A data-model comparison, *Clim. Past*, *10*(5), 1925–1938.

McGee, D., W. S. Broecker, and G. Winckler (2010), Gustiness: The driver of glacial dustiness?, *Quat. Sci. Rev.*, *29*(17), 2340–2350.

McGee, D., P. B. deMenocal, G. Winckler, J. B. W. Stuut, and L. I. Bradtmiller (2013), The magnitude, timing and abruptness of changes in North African dust deposition over the last 20,000 yr, *Earth Planet. Sci. Lett.*, *371–372*, 163–176.

McManus, J., R. Francois, J. Gherardi, L. Keigwin, and S. Brown-Leger (2004), Collapse and rapid resumption of Atlantic meridional circulation linked to deglacial climate change, *Nature*, *428*, 834–837.

Meckler, A. N., D. M. Sigman, K. A. Gibson, R. Francois, A. Martinez-Garcia, S. L. Jaccard, U. Rohl, L. C. Peterson, R. Tiedemann, and G. H. Haug (2013), Deglacial pulses of deep-ocean silicate into the subtropical North Atlantic Ocean, *Nature*, *495*(7442), 495–498.

Mittelstaedt, E. (1991), The ocean boundary along the northwest African coast: Circulation and oceanographic properties at the sea surface, *Prog. Oceanogr.*, *26*(4), 307–355.

Mortlock, R. A., and P. N. Froelich (1989), A simple method for the rapid-determination of biogenic opal in pelagic marine sediments, *Deep Sea Res., Part I*, *36*(9), 1415–1426.

Mulitza, S., M. Prange, J. B. Stuut, M. Zabel, T. von Dobeneck, A. C. Itambi, J. Nizou, M. Schulz, and G. Wefer (2008), Sahel megadroughts triggered by glacial slowdowns of Atlantic meridional overturning, *Paleoceanography*, *23*, PA4206, doi:10.1029/2008PA001637.

Murphy, L. N., A. C. Clement, S. Albani, N. M. Mahowald, P. Swart, and M. M. Arienzo (2014), Simulated changes in atmospheric dust in response to a Heinrich stadial, *Paleoceanography*, *29*, 30–43, doi:10.1002/2013PA002550.

NASA Goddard Space Flight Center, Ocean Ecology Laboratory, Ocean Biology Processing Group (2014), *SeaWiFS Ocean Color Data*, edited by O. E. L. NASA Goddard Space Flight Center, Ocean Biology Processing Group.

Ndeye, M. (2008), Marine reservoir ages in northern Senegal and Mauritania coastal waters, *Radiocarbon*, *50*(2), 281–288.

Nelson, D. M., P. Treguer, M. A. Brzezinski, A. Leynaert, and B. Queguiner (1995), Production and dissolution of biogenic silica in the ocean—Revised global estimates, comparison with regional data and relationship to biogenic sedimentation, *Global Biogeochem. Cycles*, *9*(3), 359–372, doi:10.1029/95GB01070.

Neuer, S., V. Ratmeyer, R. Davenport, G. Fischer, and G. Wefer (1997), Deep water particle flux in the Canary Island region: Seasonal trends in relation to long-term satellite derived pigment data and lateral sources, *Deep Sea Res., Part I*, *44*(8), 1451–1466.

Paillard, D., L. Labeyrie, and P. Yiou (1996), Macintosh program performs time-series analysis, *Eos Trans. AGU*, *77*(39), 379–379, doi:10.1029/96EO00259.

Patricola, C. M., and K. H. Cook (2007), Dynamics of the West African monsoon under mid-Holocene precessional forcing: Regional climate model simulations, *J. Clim.*, *20*(4), 694–716.

Peterson, L. C., G. H. Haug, K. A. Hughen, and U. Rohl (2000), Rapid changes in the hydrologic cycle of the tropical Atlantic during the last glacial, *Science*, *290*(5498), 1947–1951.

Prell, W. L., and J. E. Kutzbach (1987), Monsoon variability over the past 150,000 years, *J. Geophys. Res.*, *92*(D7), 8411–8425, doi:10.1029/JD092iD07p08411.

Ragueneau, O., et al. (2000), A review of the Si cycle in the modem ocean: Recent progress and missing gaps in the application of biogenic opal as a paleoproductivity proxy, *Global Planet. Change*, *26*(4), 317–365.
Ratmeyer, V., G. Fischer, and G. Wefer (1999), Lithogenic particle fluxes and grain size distributions in the deep ocean off northwest Africa: Implications for seasonal changes of aeolian dust input and downward transport, *Deep Sea Res., Part I*, *46*(8), 1289–1337.
Rea, D. K. (1994), The paleoclimatic record provided by eolian deposition in the deep sea: The geologic history of wind, *Rev. Geophys.*, *32*(2), 159–195, doi:10.1029/93RG03257.
Reimer, P. J., et al. (2013), IntCal13 and Marine13 radiocarbon age calibration curves 0–50,000 years cal BP, *Radiocarbon*, *55*, 1869–1887.
Ridley, D. A., C. L. Heald, and J. M. Prospero (2014), What controls the recent changes in African mineral dust aerosol across the Atlantic?, *Atmos. Chem. Phys. Discuss.*, *14*(3), 3583–3627.
Romero, O. E., J. H. Kim, and B. Donner (2008), Submillennial-to-millennial variability of diatom production off Mauritania, NW Africa, during the last glacial cycle, *Paleoceanography*, *23*, PA3218, doi:10.1029/2008PA001601.
Roskin, J., H. Tsoar, N. Porat, and D. G. Blumberg (2011), Palaeoclimate interpretations of Late Pleistocene vegetated linear dune mobilization episodes: Evidence from the northwestern Negev dunefield, Israel, *Quat. Sci. Rev.*, *30*(23–24), 3364–3380.
Sarmiento, J. L., N. Gruber, M. A. Brzezinski, and J. P. Dunne (2004), High-latitude controls of thermocline nutrients and low latitude biological productivity, *Nature*, *427*(1), 56–60.
Sarnthein, M., G. Tetzlaff, B. Koopmann, K. Wolter, and U. Pflaumann (1981), Glacial and interglacial wind regimes over the eastern subtropical Atlantic and North-West Africa, *Nature*, *293*(5829), 193–196.
Scholten, J. C., J. Fietzke, S. Vogler, M. M. R. van der Loeff, A. Mangini, W. Koeve, J. Waniek, P. Stoffers, A. Antia, and J. Kuss (2001), Trapping efficiencies of sediment traps from the deep Eastern North Atlantic: The Th-230 calibration, *Deep Sea Res., Part II*, *48*(10), 2383–2408.
Scholten, J. C., et al. (2005), Radionuclide fluxes in the Arabian Sea: The role of particle composition, *Earth Planet. Sci. Lett.*, *230*(3–4), 319–337.
Shanahan, T. M., N. P. McKay, K. A. Hughen, J. T. Overpeck, B. Otto-Bliesner, C. W. Heil, J. King, C. A. Scholz, and J. Peck (2015), The time-transgressive termination of the African Humid Period, *Nat. Geosci.*, *8*(2), 140–144.
Skonieczny, C., A. Bory, V. Bout-Roumazeilles, W. Abouchami, S. Galer, X. Crosta, J. B. Stuut, I. Meyer, I. Chiapello, and T. Podvin (2011), The 7–13 March 2006 major Saharan outbreak: Multiproxy characterization of mineral dust deposited on the West African margin, *J. Geophys. Res.*, *116*, D18210, doi:10.1029/2011JD016173.
Stager, J. C., D. B. Ryves, B. M. Chase, and F. S. R. Pausata (2011), Catastrophic Drought in the Afro-Asian monsoon region during Heinrich event 1, *Science*, *331*(6022), 1299–1302.
Street-Perrott, F. A., and R. A. Perrott (1990), Abrupt climate fluctuations in the tropics—the influence of Atlantic Ocean Circulation, *Nature*, *343*(6259), 607–612.
Street-Perrott, F. A., and R. A. Perrott (1993), Holocene vegetation, lake levels and climate in Africa, in *Global Climates Since the Last Glacial Maximum*, edited by H. E. Wright et al., pp. 318–356, Univ. of Minnesota, Minneapolis, Minn.
Street-Perrott, F. A., and S. P. Harrison (1984), Temporal variations in lake levels since 30,000 yr BP—an index of the global hydrological cycle, in *Climate Processes and Climate Sensitivity*, edited by J. E. Hansen and T. Takahashi, pp. 118–129, AGU, Washington, D. C.
Tierney, J. E., and P. B. deMenocal (2013), Abrupt shifts in Horn of Africa hydroclimate since the Last Glacial Maximum, *Science*, *342*(6160), 843–846.
Tjallingii, R., M. Claussen, J.-B. W. Stuut, J. Fohlmeister, A. Jahn, T. Bickert, F. Lamy, and U. Rohl (2008), Coherent high- and low-latitude control of the northwest African hydrological balance, *Nat. Geosci.*, *1*(10), 670–675.
Todd, M. C., R. Washington, J. V. Martins, O. Dubovik, G. Lizcano, S. M'Bainayel, and S. Engelstaedter (2007), Mineral dust emission from the Bodélé Depression, northern Chad, during BoDEx 2005, *J. Geophys. Res.*, *112*, D06207, doi:10.1029/2006JD007170.
Tréguer, P. J., and C. L. De La Rocha (2013), The world ocean silica cycle, *Annu. Rev. Mar. Sci.*, *5*, 477–501.
Treguer, P., D. M. Nelson, A. J. Vanbennekom, D. J. Demaster, A. Leynaert, and B. Queguiner (1995), The silica balance in the world ocean: A reestimate, *Science*, *268*(5209), 375–379.
Tsoar, H. (2005), Sand dunes mobility and stability in relation to climate, *Phys. A*, *357*(1), 50–56.
Van Camp, L., L. Nykjaer, E. Mittelstaedt, and P. Schlittenhardt (1991), Upwelling and boundary circulation off Northwest Africa as depicted by infrared and visible satellite observations, *Prog. Oceanogr.*, *26*(4), 357–402.
Walczak, I. W., J. U. Baldini, L. M. Baldini, F. McDermott, S. Marsden, C. D. Standish, D. A. Richards, B. Andreo, and J. Slater (2015), Reconstructing high-resolution climate using CT scanning of unsectioned stalagmites: A case study identifying the mid-Holocene onset of the Mediterranean climate in southern Iberia, *Quat. Sci. Rev.*, *127*, 117–128.
Wanner, H., et al. (2008), Mid- to Late Holocene climate change: An overview, *Quat. Sci. Rev.*, *27*(19–20), 1791–1828.
Weldeab, S., D. W. Lea, R. R. Schneider, and N. Andersen (2007), 155,000 years of West African monsoon and ocean thermal evolution, *Science*, *316*(5829), 1303–1307.
Weldeab, S., M. Frank, T. Stichel, B. Haley, and M. Sangen (2011), Spatio-temporal evolution of the West African monsoon during the last deglaciation, *Geophys. Res. Lett.*, *38*, L13703, doi:10.1029/2011GL047805.
Weldeab, S., V. Menke, and G. Schmiedl (2014), The pace of East African monsoon evolution during the Holocene, *Geophys. Res. Lett.*, *41*, 1724–1731, doi:10.1002/2014GL059361.
Yokomizo, H., L. W. Botsford, M. D. Holland, C. A. Lawrence, and A. Hastings (2010), Optimal wind patterns for biological production in shelf ecosystems driven by coastal upwelling, *Theor. Ecol.*, *3*(1), 53–63.
Yu, E. F., R. Francois, M. P. Bacon, and A. P. Fleer (2001), Fluxes of Th-230 and Pa-231 to the deep sea: Implications for the interpretation of excess Th-230 and Pa-231/Th-230 profiles in sediments, *Earth Planet. Sci. Lett.*, *191*(3–4), 219–230.
Zarriess, M., and A. Mackensen (2010), The tropical rainbelt and productivity changes off northwest Africa: A 31,000-year high-resolution record, *Mar. Micropaleontol.*, *76*(3–4), 76–91.
Zhang, H.-M., J. J. Bates, and R. W. Reynolds (2006), Assessment of composite global sampling: Sea surface wind speed, *Geophys. Res. Lett.*, *33*, L17714, doi:10.1029/2006GL027086.
Zhang, R., and T. L. Delworth (2005), Simulated tropical response to a substantial weakening of the Atlantic thermohaline circulation, *J. Clim.*, *18*(12), 1853–1860.
Zhao, M. X., J. L. Mercer, G. Eglinton, M. J. Higginson, and C. Y. Huang (2006), Comparative molecular biomarker assessment of phytoplankton paleoproductivity for the last 160 kyr off Cap Blanc, NW Africa, *Org. Geochem.*, *37*(1), 72–97.
Zhao, M., N. A. S. Beveridge, N. J. Shackleton, M. Sarnthein, and G. Eglinton (1995), Molecular stratigraphy of cores off Northwest Africa: Sea surface temperature history over the last 80 ka, *Paleoceanography*, *10*(3), 661–675, doi:10.1029/94PA03354.
Zhao, M., H. Eglinton, M. S. Jordan, and Z. Zhang (2000), Marine and terrestrial biomarker records for the last 35,000 years at ODP site 658C off NW Africa, *Org. Geochem.*, *31*(9), 919–930.